JOURNAL OF GEOPHYSICAL RESEARCH, VOL. 113, E02004, doi:10.1029/2007JE002893, 2008

Dust haze in Valles Marineris observed by HRSC and OMEGA on board Mars Express

A. Inada,[1] M. Garcia-Comas,[2] F. Altieri,[3] K. Gwinner,[4] F. Poulet,[5] G. Bellucci,[3] H. U. Keller,[2] W. J. Markiewicz,[2] M. I. Richardson,[1] N. Hoekzema,[2] G. Neukum,[6] and J.-P. Bibring[5]

Received 9 January 2007; revised 19 April 2007; accepted 11 October 2007; published 9 February 2008.

[1] We present analysis of a bright haze observed inside Valles Marineris, which formed in mid northern spring. The data were collected by the High Resolution Stereo Camera (HRSC) and the imaging spectrometer, Observatoire pour la Minéralogie, l'Eau, les Glaces et l'Activité (OMEGA), aboard Mars Express. This study provides a case example of the power of simultaneous multiple emission angle and hyperspectral imaging for study of aerosols and clouds in the Martian atmosphere. The haze appeared thinner after three days and disappeared in nine days. It was limited to a 2-km layer at the bottom of the canyon. The color was redder than the underlying surface. The analysis of the OMEGA spectra indicates that this haze was composed of dust particles. The dust layer appeared brighter with the HRSC stereo channels than the nadir channel due to longer scattering paths. We have estimated the optical depth of the haze by fitting both HRSC and OMEGA data with radiative transfer calculations. The retrieval of the optical depth is very sensitive to the aerosol scattering model used and the reflectance of the surface. Applying an aerosol scattering model derived from sky surveys at a constant elevation by the Imager for Mars Pathfinder, the optical depth of the haze is estimated from HRSC data to be within 1.7 to 2.3 at the wavelength (λ) of 0.675 μm. The wavelength dependence is obtained from OMEGA spectrum. It increases to 2.2–2.6 at λ = 1.35 μm and moderately decreases to 1.2–1.8 at λ = 2.4 μm.

Citation: Inada, A., et al. (2008), Dust haze in Valles Marineris observed by HRSC and OMEGA on board Mars Express, *J. Geophys. Res.*, *113*, E02004, doi:10.1029/2007JE002893.

1. Introduction

[2] Valles Marineris, located near the equator, is the deepest valley system on Mars. Its depth reaches up to 8 km and its length extends from 270°E to 310°E. This great canyon affects the atmosphere on a global scale. It is known that the main cloud belt appears constantly over the valley in late northern spring and summer (or "aphelion season") [e.g., *Wang and Ingersoll*, 2002]. This region is also particularly interesting for the study of atmospheric behavior on mesoscales due to the extreme variation of topography.

[3] Although the High Resolution Stereo Camera (HRSC) aboard Mars Express (MEX) has been primarily designed to map the surface of Mars, it can also be used to study various aspects of the Martian atmosphere [*Neukum and Jaumann*, 2004]. The stereo channels detect the scattered light at five geometric angles with different path lengths. The angular dependences of the surface and the aerosol scattering behaviors, as well as the optical thickness of the atmosphere influence the stereo data. Observatoire pour la Minéralogie, l'Eau, les Glaces et l'Activité (OMEGA), an imaging spectrometer on MEX, was designed primarily to study surface mineralogy. It has identified a variety of mafic and altered minerals [*Bibring et al.*, 2004, 2006] and H_2O/CO_2 ice on the south polar cap [*Bibring et al.*, 2004]. Moreover, temperature and pressure at the surface can be derived from the spectra [*Forget et al.*, 2007; *Melchiorri et al.*, 2006] and, as it will be shown here, also the composition of atmospheric features such as clouds or hazes. The combination of these two instruments provides useful data sets for detailed study of local weather on Mars that has been unavailable before the arrival of Mars Express. Future spacecraft will have the ability to use the techniques described in this paper, including the Mars Reconnaissance Orbiter. For example, imaging data can show the spatial distribution of atmospheric hazes; however, it does not distinguish well between water ice and dust particles. The spectrometer data, on the other hand, can usually do this separation very well.

[1]Geological and Planetary Sciences, California Institute of Technology, Pasadena, California, USA.
[2]Max-Plank-Institute of Solar System Research, Lindau, Germany.
[3]Istituto di Fisica dello Spazio Interplanetario, INAF, Rome, Italy.
[4]Institute of Planetary Research, German Aerospace Center (DLR), Berlin, Germany.
[5]IAU, Université Paris, Orsay, France.
[6]Institute of Geological Sciences, Freie Universität Berlin, Berlin, Germany.

0148-0227/08/2007JE002893$09.00

[4] MEX was launched on 2 June 2003 and arrived at Mars in December 2003. In the first year of operation, the instruments observed a bright haze in Valles Marineris. The HRSC data show the appearance of the haze to depend on time of day. The observations motivated us to research a local atmospheric activity in short timescale to understand the Martian atmosphere better in mesoscale level. The spectra taken with OMEGA show that it consists of dust particles, although one may easily consider that it is a water ice fog. The formation processes of the haze are still unknown; however, it seems plausible that the haze could be generated inside the canyon due to strong winds. The detailed studies of the dust haze will constrain the future work about examination of potential processes of dust lifting. Besides, the spectral dependence of the reflectance measured over this thick haze layer is dominated by the nature of the aerosols of which it is composed. Therefore the analysis of these measurements provides a chance to test the suitability and the sensitivity for the aerosols involved in this specific scenario against several optical property sets reported in the literature to the present day. This kind of analysis thus constrains the properties of the Martian aerosols which may be extended to a variety of situations on Mars. Here, we report on the characteristics and the estimated optical depth of the haze. We describe the instruments in section 2 and the observations in section 3. In section 4, we show the characteristics of the haze such as composition, brightness temperature, the wavelength and angular dependences of the haze reflectance, haze height, and optical depth. The conclusions are summarized in section 5.

2. Instruments

[5] HRSC was developed at the German Aerospace Center (DLR), Germany, in cooperation with German industry. It is a pushbroom scanner applying nine CCD line sensors observing in four colors (Blue: 440 ± 45 nm, Green: 530 ± 45 nm, Red: 750 ± 20 nm, and IR: 970 ± 45 nm) and five panchromatic stereo bands (675 ± 90 nm). During nominal observations the camera is nadir pointing, and the angles of the channels from nadir are 18.9° (S1), 15.0° (IR) 12.8° (P1), 2.4° (Green), 0° (ND), −2.4° (Blue), −12.8° (P2), −15.0° (Red), −18.9° (S2) along the track. In general all channels operate simultaneously; usually pixels are summed into macro pixels for most channels to decrease the data volume before transmission. An image has a swath of 62 km with the spatial resolution of 12 m/pixel at pericenter, and the minimum length of an image is about 330 km. At true anomalies of ±20° the spatial resolution is ∼15 m/pixel [*Neukum and Jaumann*, 2004]. The preflight radiometric calibration includes pixel response nonuniformity effects of the optics, dark signal, CCD saturation behavior, spectral responsivity, camera sensitivity to gain changes, integration time and macro-pixel format, signal dependence on temperature, linearity with respect to illumination levels, stability with respect to permutations of the CCD to signal chain allocation, temporal signal stability, and sensitivity to electrical perturbations from outside the camera [*Jaumann et al.*, 2007]. Imaging of the Earth and Moon during cruise has confirmed the on-ground calibration. The signal noise ratio for panchromatic and color channels are larger than 100 and 80, respectively, except Blue with larger than 40.

[6] OMEGA was developed through the collaboration of Institut d'Astrophysique Spatiale (IAS), Orsay, France; Laboratoire d'Etudes Spatiales et d'Instrumentation en Astrophysique (LESIA), Observatoire de Paris/Meudon, France; Istituto di Fisica dello Spazio Interplanetario (IFSI), Rome, Italy; and Institute for Space Research (IKI), Moscow, Russia. OMEGA can acquire images with a spatial resolution ranging from 300 m/pixel to 5 km/pixel, depending on the position of the spacecraft on its elliptic orbit, and provide for each pixel of the image a spectrum from wavelengths (λ) of 360 nm to 5100 nm with 352 channels. The mean spectral resolution is about 15 nm and the signal-to-noise ratio is larger than 100 at all wavelengths. To cover the entire spectral range OMEGA uses three separate channels: the visible and near-infrared channel VNIR, operating from λ = 360 to 1010 nm, and two infrared channels SWIR and LWIR, operating from λ = 930 to 2650 nm and 2510 to 5100 nm, respectively [*Bibring*, 2004]. The detailed preflight calibration setup is described by *Bonello et al.* [2005] and the radiometric absolute and relative sensitivities are less than 20% and 1%, respectively.

3. Observations Over Valles Marineris

3.1. Season and the Local Time

[7] HRSC observed Valles Marineris on 25 May 2004 (the orbit number is 438), 28 May 2004 (449) and 3 June 2004 (471). The observation days, the areocentric solar longitudes (L_s), the local times, and the geometric angles are summarized in Table 1. The images of orbits 438 and 449, as well as those of orbits 449 and 471, overlap each other. They can therefore provide information on weather changes within the canyon. The observations were performed with all channels. The spacecraft moved from south to north, and S1, IR, P1 and Green channels were forward looking while Blue, P2, Red and S2 were backward looking.

[8] OMEGA obtained spectra of the same region and at the same time as HRSC on 25 May 2004 (i.e., during orbit 438). On orbits 460 (acquired on 31 May 2004) and 482 (6 June 2004) images of Valles Marineris were also taken by OMEGA (Table 1), though they were not overlapped and they were not taken simultaneously by HRSC. These were nominal nadir mode observations.

[9] All images were taken in the morning, at the local time of around 9 A.M. The difference in illumination angles is little, and hence it does not affect the comparison of the images. The images were collected at the beginning of the aphelion season (L_s = 40°) before the tropical cloud belt had extended over the valley [*Smith et al.*, 2001; *Smith*, 2004; *Wang and Ingersoll*, 2002].

3.2. Brightness Change in Valles Marineris

[10] Figure 1 shows the HRSC orthoimages of Valles Marineris, including the haze, that have been map-projected using the high-resolution HRSC digital terrain model (DTM) [*Gwinner et al.*, 2005]. HRSC level 4 orthoimages [*Scholten et al.*, 2005] are map-projected images in which geometric distortions due to topography have been eliminated using the underlying HRSC DTM. The level 4 data are resized for a suitable spatial resolution by averaging I/F

Table 1. Summary of Observations[a]

Orbit Number	Instrument	Observation Day	L_s, deg	Local Time	i, deg	e, deg	g, deg
438	HRSC	25 May 2004	38	0915	49	28 (S1), 23 (IR), 18 (P1), 6 (GR), 4 (ND), 7 (BL), 19 (P2), 24 (RE). 28 (S2)	66(S1), 63(IR), 60(P1), 51(GR), 49(ND), 46(BL), 41(P2), 40(RE), 39(S2)
438	OMEGA	25 May 2004	38	0915	49	10	49
449	HRSC	28 May 2004	40	0915	51	28(S1), 23(IR), 7(GR), 5(ND), 8(BL), 24(RE), 29(S2)	65(S1), 62(IR), 50(GR), 47(ND), 45(BL), 38(RE), 38(S2)
460	OMEGA	31 May 2004	41	0907	53	9	52
471	HRSC	3 June 2004	42	0900	53	26(S1), 22(IR), 6(GR), 4(ND), 7(BL), 25(RE), 30(S2)	67(S1), 64(IR), 54(GR), 51(ND), 49(BL), 42(RE), 41(S2)
482	OMEGA	6 June 2004	45	0857	55	12	55

[a]Notes: i, e, and g are average incidence, emission, and phase angles of the Valles Marineris data, respectively. S1, IR, P1, GR (Green), ND, BL (Blue), P2, RE (Red), and S2 denote the HRSC channels.

of some pixels on the original images depending on macro-pixel setting. This method increases radiometric accuracy typically by factor of 10 for ND data that are generally obtained without the macro-pixel mode. The lines in Figure 1 mark overlap areas between orbits 438 and 449 (white), and 449 and 471 (red). They correspond to longitudes of 301.2°E and 298.7°E, respectively.

[11] Due to the large optical depth of the haze, the observed contrast inside the valley during orbit 438 is significantly decreased and the atmospheric haze shows up quite brightly (Figure 1, right). Figure 1 (middle) displays an image of the same region, but slightly west, acquired three days later during orbit 449. There is a haze inside the valley as well, but it is relatively thinner. Six days later, as it can be seen in the HRSC image taken during orbit 471, the haze had disappeared or was too thin to detect (Figure 1, left).

[12] Figure 2 quantitatively presents the brightness change in the valley obtained with the Green channel, which represents the typical behavior of all channels. I/F profiles along the white lines of Figure 1 detected during orbits 438 and 449 are shown with the solid and dashed lines, respectively, in Figure 2 (left). Henceforth, I/F is defined as the ratio of the detected intensity to intensity reflected from a perfect Lambert surface illuminated at the zenith angle of zero degree. Figure 2 (right) shows I/F along the red line in Figure 1 of orbit 449 with the solid line and 471 with the dashed line. The altitude of the surface is plotted with the dotted lines as a reference. Latitudes between 13°S and 14°S correspond to the interior of Valles

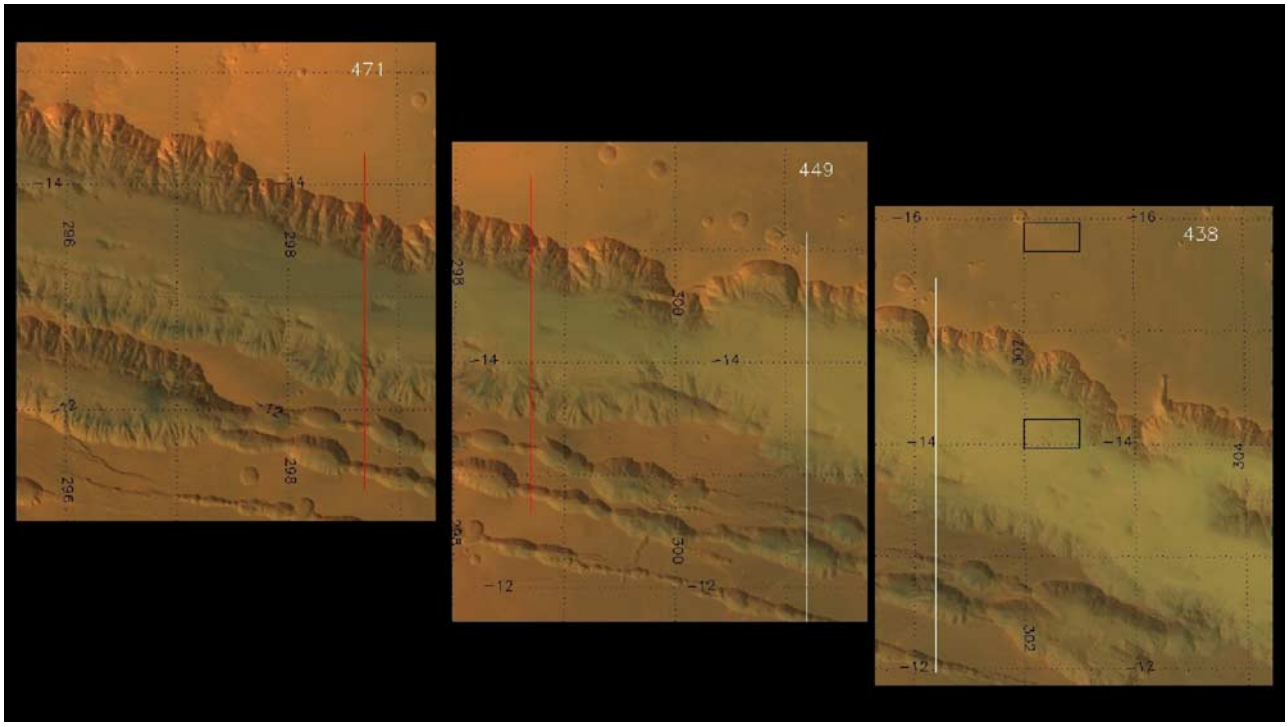

Figure 1. HRSC true color images of Valles Marineris obtained on (right) 25 May 2004 (during orbit 438, L_s = 38°, LT = 0915), (middle) 28 May 2004 (449, L_s = 40°, LT = 0915), and (left) 3 June 2004 (471, L_s = 42°, LT = 0900). The red and white lines are along longitudes of 298.7°E and 301.2°E, respectively. The boxes indicate the north region (12.00°S–12.25°S, 302.0°E–302.5°E) and the inside of the valley (13.75°S–14.00°S, 302.0°E–302.5°E).

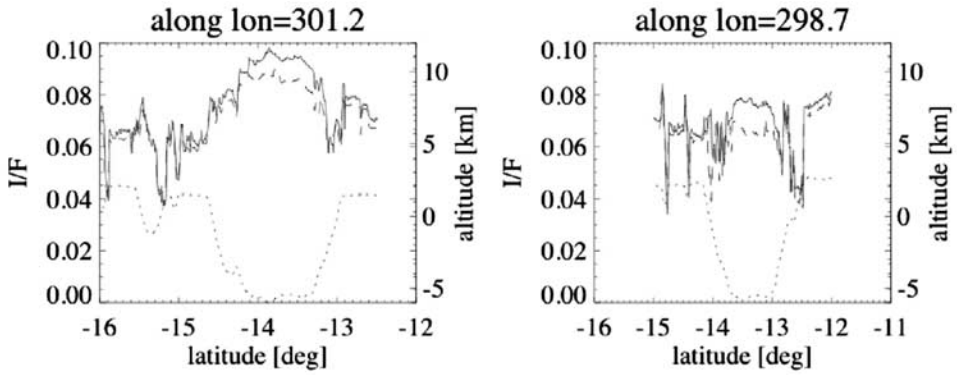

Figure 2. Brightness across Valles Marineris acquired with the HRSC Green channel. The dotted lines show the altitude for the reference. (left) I/F along the longitude of 301.2°E. Solid and dashed lines are for orbits 438 and 449. (right) I/F along the longitude of 298.8°E. Solid and dashed lines are for orbits 449 and 471.

Marineris, where I/F is larger due to the haze than outside of the valley on orbits 438 and 449. Moreover, the haze observed on orbit 438 is brighter than on orbit 449. Also the difference in I/F between the images of orbits 449 and 471 is prominent in the valley.

[13] These observations can be interpreted as the haze becoming thinner and disappearing during nine days or, alternatively, that the haze disappeared and reappeared daily, but not always with the same thickness.

3.3. Spectrum Comparison With HRSC and OMEGA in Visible Wavelength

[14] We compared the spectra from two regions of the inside of the canyon (13.75°S–14.00°S, 302.0°E–302.5°E) and a region north of the canyon (12.00°S–12.25°S, 302.0°E–302.5°E) obtained by HRSC and the OMEGA visible bands on orbit 438. The comparison provides excellent information about the absolute calibrations of the instruments because the data sets were acquired at the same time, in which the incidence angles were the same and the atmosphere was unique. The subregions are shown as the insides of the rectangles in Figure 1. OMEGA spectra of the inside and to the north of the canyon are given with the solid and dashed lines, respectively, in Figure 3, while the mean I/F of HRSC are given with the asterisks and diamonds.

[15] Inside Valles Marineris, the detected I/F by HRSC is larger than that by OMEGA except at λ = 0.675 μm, for which the data with the nadir channel are used. The HRSC data do not contain any angular correction; hence the I/F difference is likely due to the longer viewing path in the bright dust haze. The panchromatic filters have a wide spectral width of 0.18 μm, and the brightness as evidenced by OMEGA decreases steeply from the center wavelength toward the shorter wavelengths within the filter width. Therefore it is natural that the HRSC nadir data shows lower I/F than OMEGA. The measurements at this wavelength are, however, within OMEGA and HRSC one-sigma values.

[16] The data without the dust haze are more suitable to use for radiometric calibration. The response of the HRSC Blue channel is identical to those of the OMEGA I/F at the same wavelength as the ratio of HRSC I/F to OMEGA I/F ($R_{H/O}$) is 1.04. The HRSC Green and Red channels are brighter than the OMEGA data as $R_{H/O}$ = 1.18 and 1.23, respectively, while the brightness of the HRSC infrared channel is within the one-sigma of the OMEGA spectral data with $R_{H/O}$ = 0.974.

[17] The trend of our results is similar to the previous report [*McCord et al.*, 2007] except for the Green band. They compared HRSC color spectra with those from both the OMEGA visual channel and Earth-based telescope measurements for radiometric calibrations. The reflectance of the HRSC Blue, Green and IR channels agree in that of OMEGA and telescopes, while the HRSC Red I/F is systematically larger than the others. The average $R_{H/O}$ for Blue, Green, Red and IR on orbits 97, 334 and 360 data are 0.97 ± 0.02, 1.07 ± 0.02, 1.10 ± 0.03, and 0.97 ± 0.04, respectively. The differences are partially due to scattering from the atmosphere and the surface in the different viewing geometries. However, images of Phobos, which has no atmosphere, with the HRSC Red channels having similar offsets from OMEGA data implies that an instrument calibration adjustment may be needed.

[18] The $R_{H/O}$ = 1.23 at the wavelength of 0.750 μm in our data is even larger than the previously reported $R_{H/O}$ = 1.10. We attribute the differences mainly to the different observation geometries. The phase angles (g) of the north region are 38.12 degrees for the HRSC red channel. Back scattering is usually dominant for the surface, by comparison with imaging of the Moon [*Hillier et al.*, 1999]. Hence I/F of the HRSC Red is expected to be larger than OMEGA I/F that was observed at nadir with g = 48.0 degrees, unless the atmosphere is sufficiently optically thick so as to mask the surface angular behavior. The angular dependence of reflectance is further discussed in the next section. Although the reason why the HRSC Green channel is brighter over the surface than the OMEGA data in spite of the slightly larger phase angle (2.0 degrees) is still unclear, we conclude that the data collected by the two instruments agree reasonably with each other.

4. Characteristics of the Haze

4.1. Composition of the Haze

[19] The spectra taken by OMEGA during orbit 438 (Figure 3) provide insight into the composition of the haze seen in the HRSC images in Valles Marineris. The data are

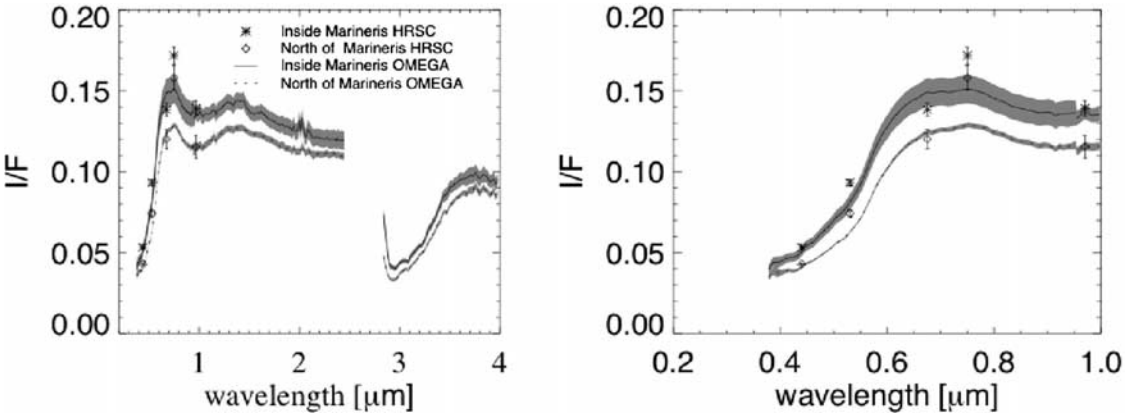

Figure 3. (left) Reflectances of the inside valley and north subregions (Figure 1) detected by OMEGA are given as the solid and dotted lines, while those obtained by HRSC are given as the asterisks and the diamonds, respectively. The thermal emission and atmospheric gaseous absorptions are corrected after *Jouglet et al.* [2007] and *Langevin et al.* [2005], respectively. The shadow areas represent one standard deviation of OMEGA data. (right) As in the left plot, but enlarged in the visible wavelength region.

corrected for thermal emission as described by *Jouglet et al.* [2007] and for atmospheric gaseous absorptions as described by *Langevin et al.* [2005].

[20] We have examined the OMEGA spectra for spectral features typical of the atmospheric aerosols most likely responsible for the increase in reflectance seen by HRSC inside the canyon. In order to discriminate airborne dust from aerosol ices, we calculated the relative band depth at 1.43 and 1.5 μm, wavelengths where CO_2 and H_2O ices show prominent absorption features [*Clark*, 1981; *Gerakines et al.*, 2005; *Warren*, 1984], we estimated the total water band depth and the water content at 3.0 μm, where H_2O ice strongly absorbs [*Bell et al.*, 1996], and we mapped the spectral slope in the near-infrared.

[21] The relative band depth at a specific wavelength λ is generally written as

$$D = 1.0 - r(\lambda)/r_c \tag{1}$$

where r(λ) is I/F at the wavelength λ and

$$r_c = (1.0 - f)\, r(\lambda_1) \; + \; fr(r_2). \tag{2}$$

λ_1 and λ_2 are the wavelength of the two points chosen for the local continuum and

$$f = (\lambda - \lambda_1)/(\lambda_2 - \lambda_1). \tag{3}$$

[22] The relative band depth is a diagnostic for the presence of atmospheric and surface constituents. A correct interpretation of the calculated relative band depths relies on an adequate selection of the continuum points. We have carefully chosen the wavelengths for the local continuum to avoid atmospheric and surface absorption features.

[23] The band at λ = 1.43 μm corresponds to absorption from CO_2 ice and gas. Figure 4a shows a 2-D map of the band depth relative to a local continuum at λ_1 = 1.39 μm and λ_2 = 1.44 μm for the portion of orbit 438 taken by OMEGA over Valles Marineris. The results are also plotted for orbit 482 to have a reference scenario without haze (Figure 4b). OMEGA spectra present a slightly stronger absorption for lower altitudes, especially for orbit 482 inside the valley. This feature could be attributable to errors in the estimated CO_2 column density used to correct the data for gas absorptions and not to CO_2 ice absorption. Besides, the fluctuations in band depth within one orbit are smaller than 2%, which should not be taken as an evidence of absorption but probably being due to the instrumental and calibration errors. Therefore we take the 1.43 μm band depth maps of both orbits to show no CO_2 ice absorption.

[24] The relative band depth at λ = 1.50 μm for orbit 438 data is shown in Figure 5a. A similar map for orbit 482 is also shown in Figure 5b for comparison. In this case, we have chosen λ_1 = 1.30 μm and λ_2 = 1.71 μm as the local continuum wavelengths. This band is sensitive to atmospheric water ice particles especially those which radii are larger than ~5.0 μm. Although OMEGA relative calibration error is less than 1%, some hysteresis affect the accuracy in the wavelength region of 1.0–1.4 μm. Hence, to account for instrumental and atmospheric biases, we consider that the water ice feature in this absorption band has to be larger than 2% to be taken as a positive detection and therefore larger than the instrumental noise. If water ice clouds were present, the band depth would be larger than under clear atmospheric conditions. On the contrary, the maps shown in Figure 5 look homogeneous and show band depths smaller than 2% across the whole plotted area. This indicates no correlation between H_2O ice and the bright feature detected in the visible wavelengths.

[25] The 3.0 μm band is a deeper and wider H_2O ice band than the one at 1.50 μm, in which both absorptions from surface hydrated minerals and atmospheric H_2O ice particles contribute. This absorption band is more sensitive to the water ice particles with radii smaller than ~3.0 μm than the 1.5 μm band [see, e.g., *Pimentel et al.*, 1974]. However, the water ice absorption in this band overlaps the surface hydration band, and thus to confidently rule out ice presence, both bands should be checked. Due to the nonlinearity of the instrument in this wavelength region, we consider that OMEGA detects water ice particles when the variation in the absorption at the 3.0 μm band is larger than 3.0%.

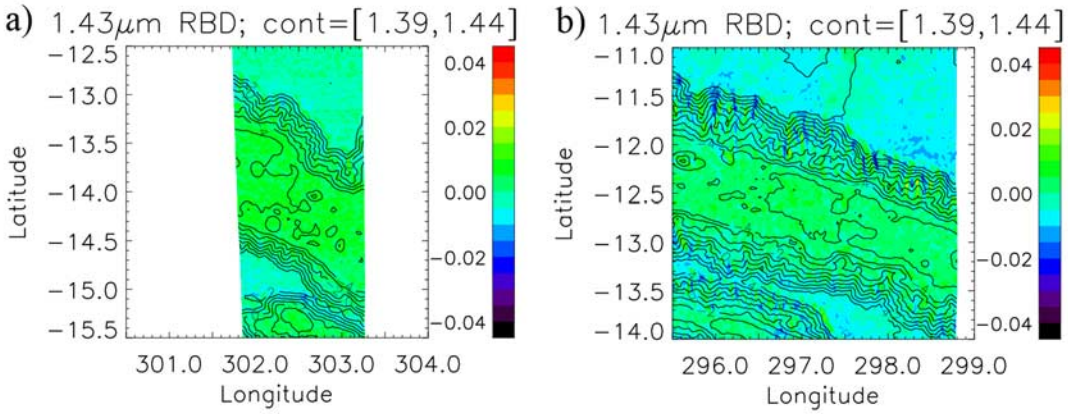

Figure 4. Relative band depth maps around Valles Marineris at wavelength of the CO_2 ice absorption band at 1.43 μm acquired by OMEGA during orbits (a) 438 and (b) 482. The wavelengths chosen for the local continuum are 1.39 and 1.44 μm.

Figure 6 shows the hydration estimated for orbits 438 and 482 by an integration of the band depth between a continuum and the spectrum from 3.0 to 3.7 μm, as described by *Jouglet et al.* [2007]. A method to retrieve the water mass proportion has been proposed by *Yen et al.* [1998], which is based on spectra measurements of Martian-like samples with several hydration rates in laboratory. The results estimated using a similar method are presented in Figure 7. It shows that there is not a significant variation of water content (less than 3.0%) between regions inside and outside the canyon. The water content maps even show slightly smaller values inside the valley when the haze was present (orbit 438). In any case, with such small variations of water content, it can be said that no water ice in the atmosphere was detected during these observations. We therefore rule out H_2O ice as the main component of the haze monitored inside Valles Marineris.

[26] The spectral slope ("reddening") in the near-infrared (NIR) is related to aerosol presence, in particular, to dust. In the NIR, the surface albedo weakly depends on wavelength (with the exception of polar regions), i.e., the spectrum of the surface component is more or less flat. However, the dust extinction cross section generally decreases with wavelength (at least beyond around 1.2–1.4 μm for the Martian dust, being that wavelength dependent on the particle size distribution). As a consequence, when dust particles are added to the atmosphere, the spectrum becomes steeper [*Drossart et al.*, 1991; *Erard et al.*, 1994]. This is also expected for water ice particles with the effective particle radii of ~1.0 μm. We define here the reddening as the ratio of reflectance at 1.26 μm to that at 2.49 μm. The reddening 2-D plots for orbits 438 and 482 over the canyon are shown in Figure 8. The footprints with topographic slopes larger than 17% (walls of the valley and abrupt regions) have been removed to avoid dependence of spectral slope on observation geometry [*Combes et al.*, 1991]. There is a correlation between the reddening and the aerosols seen in the HRSC and visible OMEGA data. The ratio is clearly larger for orbit 438 inside the canyon than that for orbit 482. Therefore, since we have already ruled out the possibility of ice particles from the data, we conclude that the composition of the haze is most likely dust.

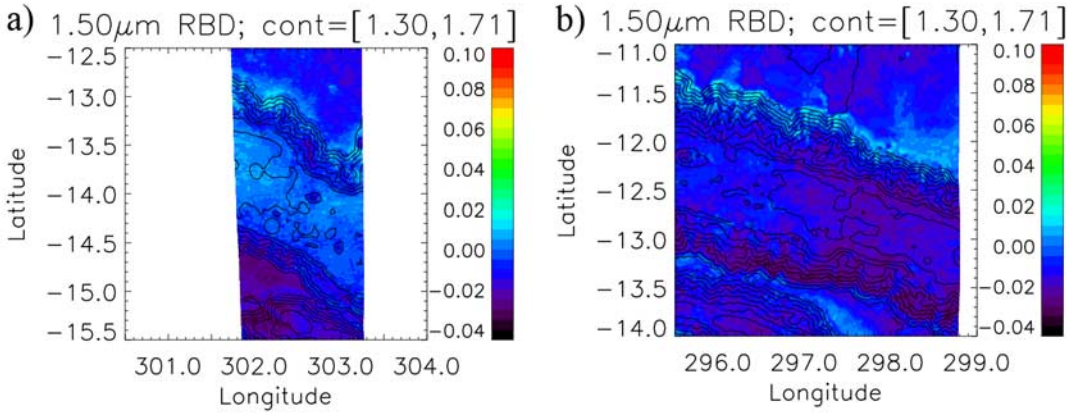

Figure 5. Relative band depth maps of the H_2O ice absorption band at 1.50 μm acquired by OMEGA during orbits (a) 438 and (b) 482 over Valles Marineris. The band depth is smaller than 2%, which indicates that no water ice was detected.

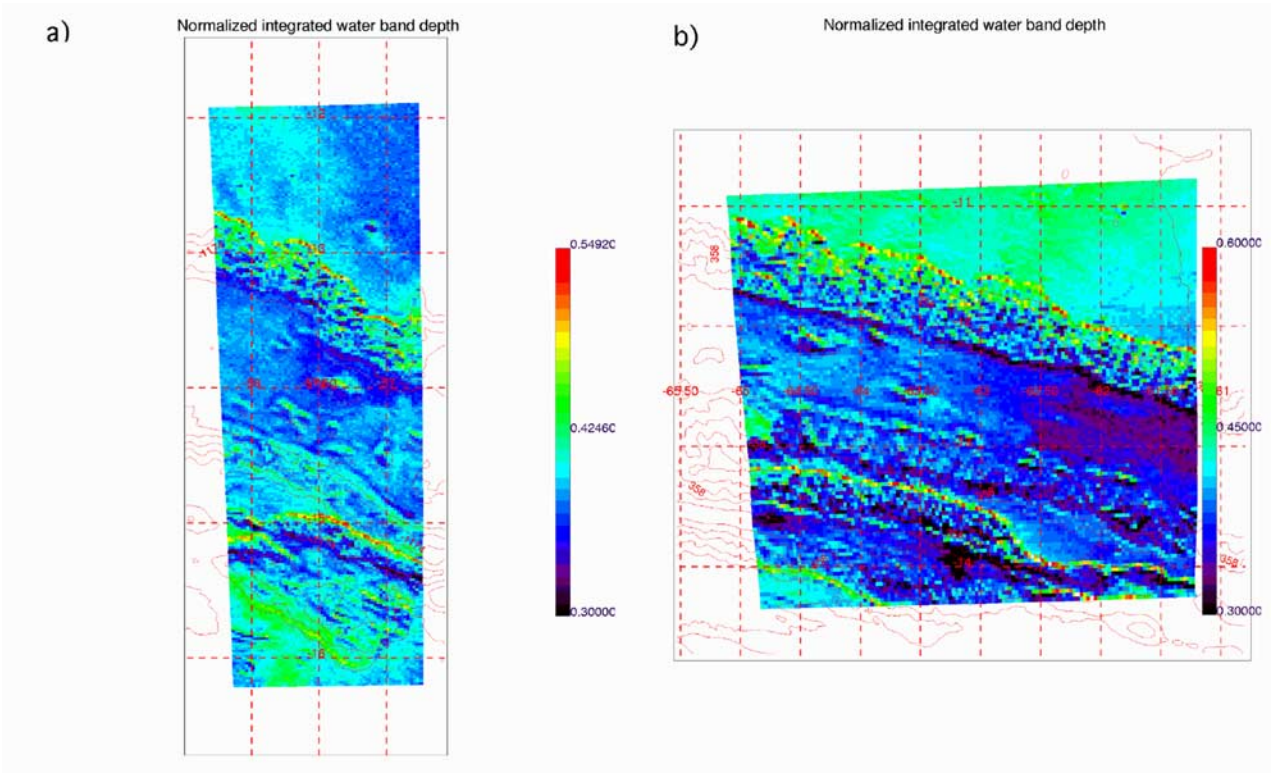

Figure 6. Normalized integrated water band depth at the wavelength of 3.0 μm observed during orbits (a) 438 and (b) 482. They include the information of the hydration of the surface and the water amount over it. The variation between inside and outside of the valley is less than 3%.

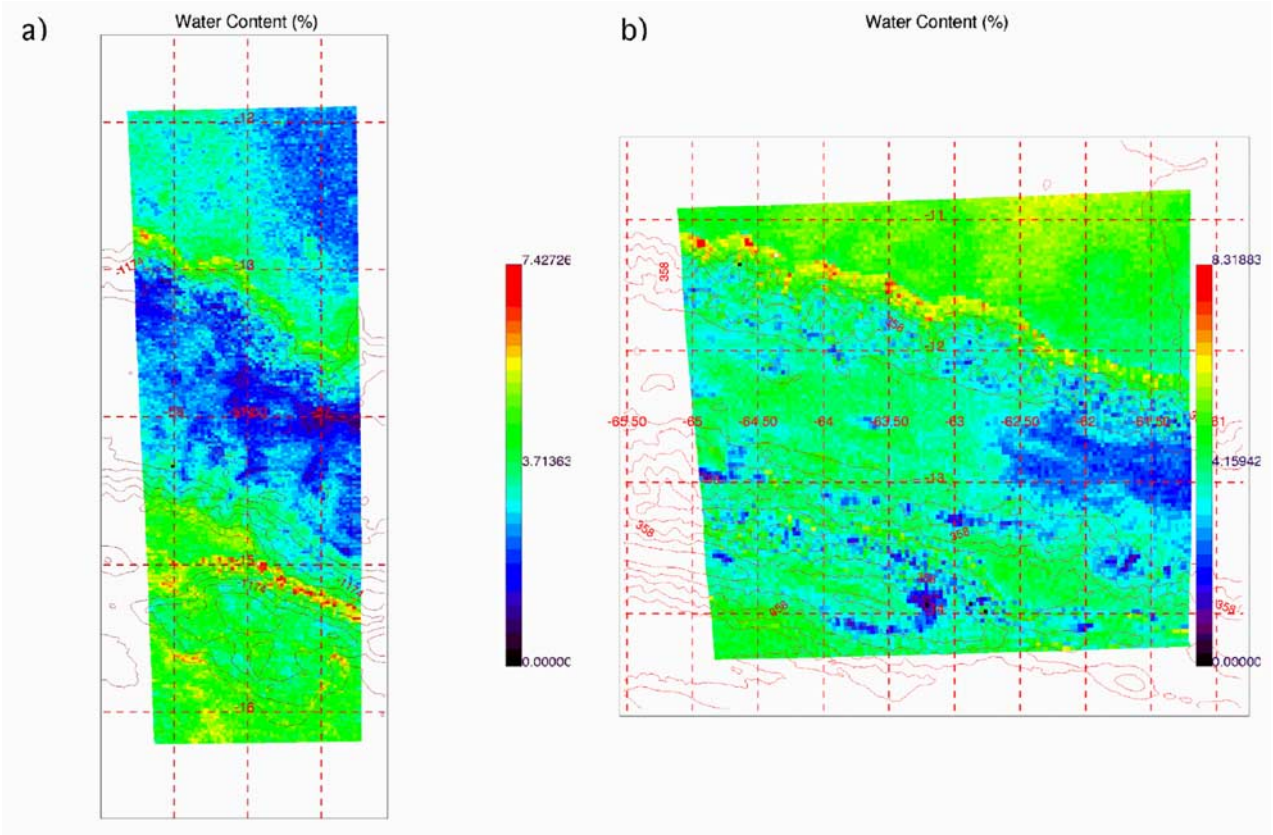

Figure 7. Water content of the surface and the atmosphere detected at the wavelength of 3.0 μm during orbits (a) 438 and (b) 482. Its variation over this area is less than 3%.

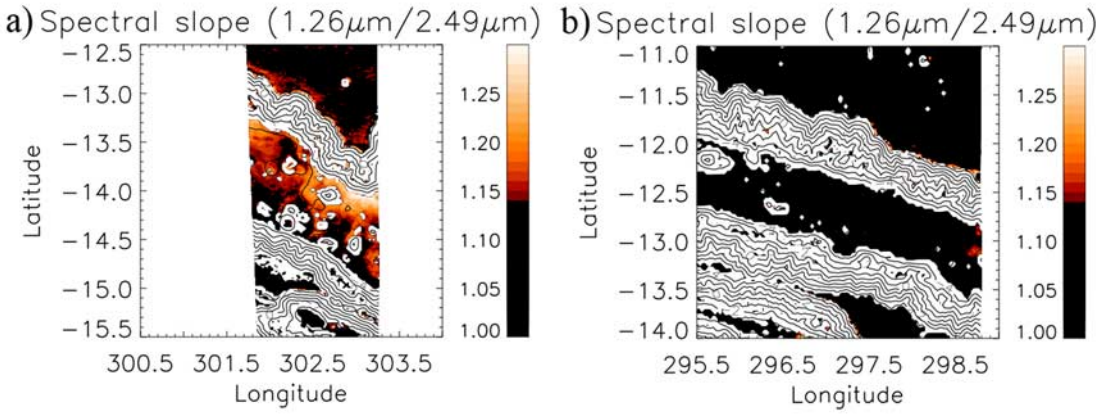

Figure 8. The ratio of I/F at 1.26 μm to I/F at 2.49 μm measured by OMEGA during orbits (a) 438 and (b) 482. A sharp decrease in I/F with wavelength in the NIR is an indication of dust loading. Orbit 438 presents a clearly steeper (negative) slope in the spectra where HRSC detected the haze inside Valles Marineris.

4.2. Valles Marineris Temperatures

[27] Another hint of ice nonpresence can be inferred from the temperature. We derived the brightness temperature at the local time of 08:57 (orbit 482), 09:07 (460) and 09:15 (438) from the OMEGA spectrum at the wavelength of 5.0 μm. Those of the inside of the canyon and the outside (north of Valles Marineris) are plotted as a function of local time in Figure 9. The temperatures are the averaged values in 0.1 × 0.1 degree boxes at the longitudes of 302.10°E, 298.94°E, 298.73°E for orbit 438, 462, and 482, respectively. The temperature outside the canyon shows an increasing trend with the local time, mainly due to an increase in the surface temperature as the sun rises. However, the inside of the canyon on orbit 438 remains colder than orbit 460, the latter orbiting at an earlier local time. This is because the brightness temperature in the canyon observed during orbit 438 is strongly affected by the temperature of the colder haze layer.

[28] Although the dust layer is colder than the surface would be if the haze layer were not present, the brightness temperature is still 223.77 ± 0.53 K. Since the dust haze is thick and it forms at low altitudes as shown in section 4.4, it can be considered that the temperature of the haze is dominant in determining the brightness temperature. In this case, it is too warm to expect any water ice particles on the basis of reasonable water vapor mass mixing ratio estimates, which supports the idea that the haze is composed of dust.

4.3. Wavelength and Angular Dependences of the Haze

[29] We compared the haze color in the overlap regions of the HRSC images. Two areas were selected: the first, at 14.25 ± 1.75°S, 301.20 ± 0.50°E, imaged during orbits 438

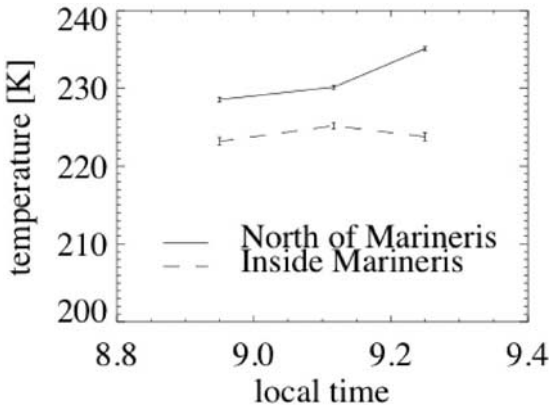

Figure 9. Brightness temperature versus local time derived with the thermal corrected data measured by OMEGA. The selected longitudes are 302.10°E, 298.94°E, and 298.73°E for orbits 438 (local time 0915), 460 (0907), and 482 (0853), respectively. The brightness temperature is averaged in 0.1 × 0.1 degree boxes. The error bars represent 1-sigma standard deviation. The brightness temperatures of the north and inside of the valley are shown as the solid and dashed lines, respectively.

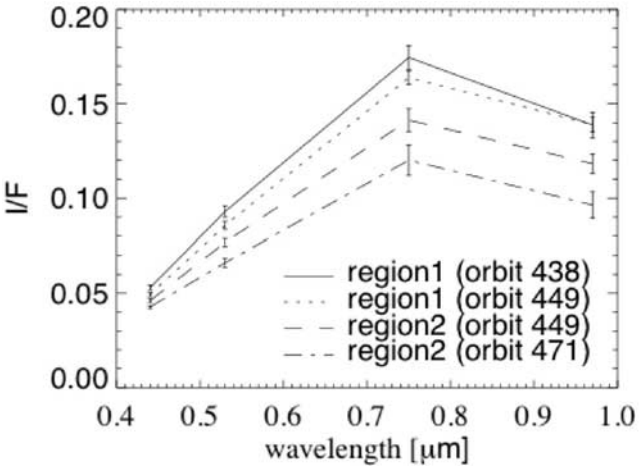

Figure 10. I/F color slopes of region 1 observed by HRSC on orbits 438 (solid line) and 449 (dotted) and region 2 on orbits 449 (dashed) and 471 (dot-dashed). Two images overlapped these regions. Regions 1 and 2 are at 14.25 ± 1.75°S, 301.2 ± 0.5°E and 13.5 ± 1.5°S, 298.7 ± 0.5°E, respectively. The error bars show 1-sigma level.

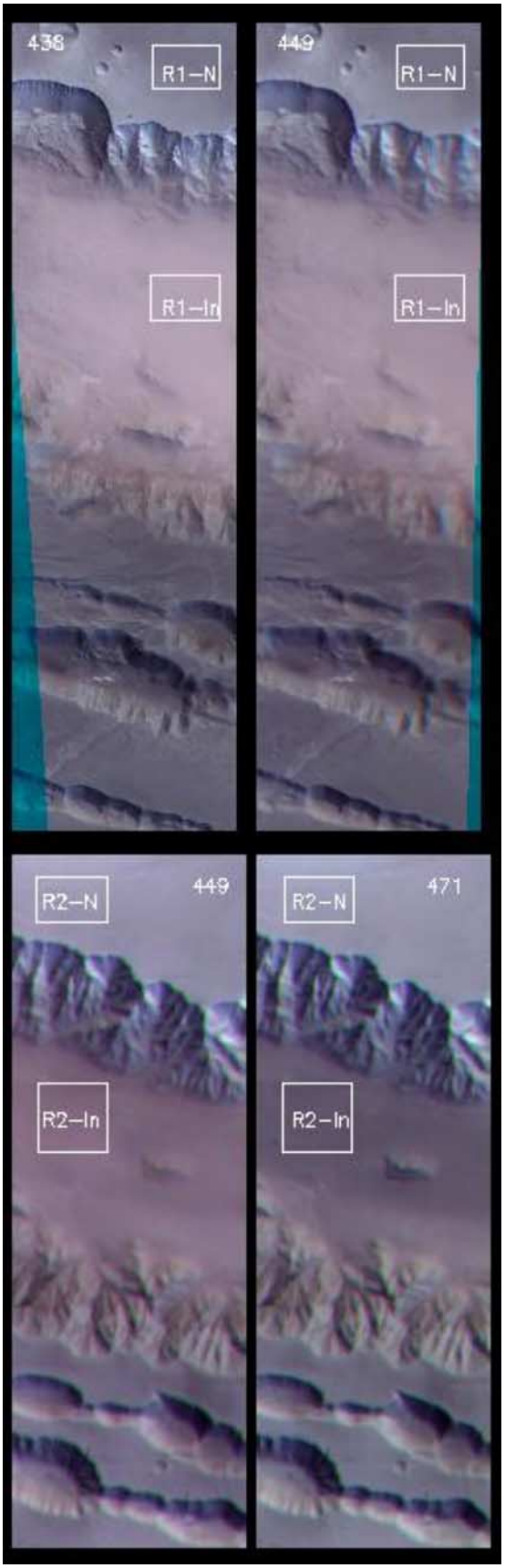

and 449 (hereafter referred as region 1), and the second, at 13.50 ± 1.50°S, 298.70 ± 0.50°E, was imaged during orbits 449 and 471 (region 2). The center longitudes are indicated with the white (region 1) and red (region 2) lines in Figure 1. These are the different regions from the areas that we used for the spectra comparison between HRSC and OMEGA, because we have to select overlap regions of the HRSC data taken on different orbits for this purpose. We used only pixels corresponding to surface elevations of less than −5000 m for the color analysis.

[30] The color slopes of the considered regions are shown in Figure 10. Region 2, which includes dust haze (orbit 449), has a markedly different wavelength dependence from the surface in the absence of haze (orbit 471 image). The ratio R = r(0.75)/r(0.44) increases from 2.8 (clear atmosphere) to 3.1 (with the dust). The haze is thicker in region 1 on the same image (449) and R = 3.3. This suggests that dust particles redden the total radiance in visible wavelength. The haze observed on orbit 438 is even thicker and brighter than on orbit 449; however, the color ratio r is the same.

[31] Figure 11 shows color-composite stereo views of regions 1 observed on orbits 438 and 449 and region 2 obtained on orbits 449 and 471. These were created using panchromatic channels as red for S1, green for nadir and blue for S2. The phase angles are 36.3 (S2), 46.0 (ND) and 62.4 (S1) degrees for region 1 on orbit 438, respectively, while they are 40.7, 50.9 and 66.9 degrees for region 1 on orbit 449. In region 2 the angles are 34.7 (S2), 43.7 (ND) and 60.4 (S1) degrees for orbit 449, and 43.0 (S2), 53.2 (ND) and 69.1 (S1) degrees for orbit 471. There is an obvious false color difference between the inside and outside of the canyon, highlighting different angular dependences. The bluish surface indicates the strong back scattering.

[32] The angular dependence of I/F for the haze and the surface are given in Figure 12. These areas are marked as the white boxes (0.3° × 0.2°) in Figure 11. In each region 1 and 2, we have selected two subareas for the haze and the surface. Only the data from the panchromatic channels were analyzed to avoid wavelength dependence. The brightness of the haze in region 1 slightly increases with increasing emission angle (*e*), which is due to the longer path length in the haze (Figure 12a). The thinner haze in region 2 (orbit 449) also shows minimum I/F at the smallest *e*, i.e., with the shortest path length. The surface scattering function plotted against *e* for the HRSC image data obtained on orbit 438 has a strange zigzag pattern (Figure 12b). It is due to the surface phase function that is not masked by the thin atmospheric opacity. This is not seen in data from other orbits because P1 and P2 data are not available. On the other

Figure 11. Color-composite stereo images of region 1 of (top left) orbit 438 and (top right) orbit 449 and region 2 of (bottom left) orbit 449 and (bottom right) orbit 471. S1 is red, nadir is green, and S2 is blue. The rectangles are selected regions to compare I/F of inside and outside Valles Marineris. R1-N and R1-In denote the areas north of and inside Valles Marineris in region 1, respectively, while R2-N and R2-In are for the areas north of and inside the valley in region 2.

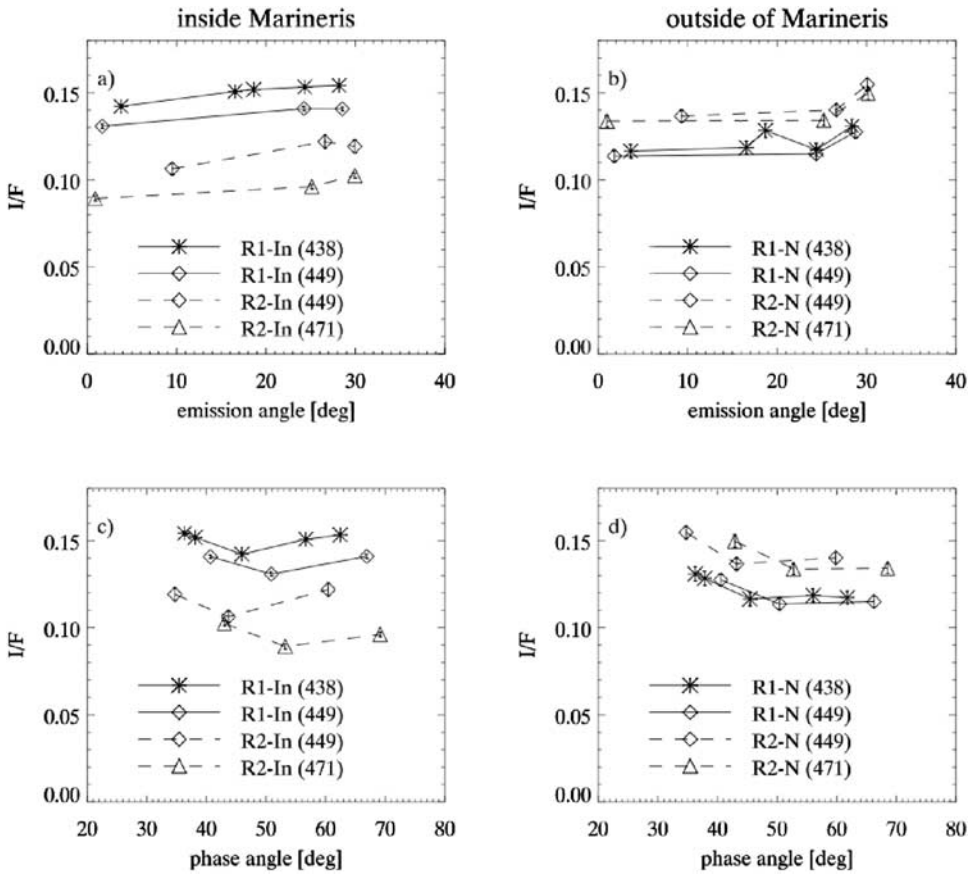

Figure 12. The angular dependences of the reflectance from region 1 in orbit 438 (the solid line with asterisks) and orbit 449 (the solid line with diamonds) and region 2 in orbit 449 (the dashed line with diamonds) and orbit 471 (the dashed line with triangles) detected by HRSC. Figures 12a and 12b show the emission angle dependence, while Figures 12c and 12d show the phase angle dependence. Figures 12a and 12c give the mean I/F only inside the valley (given as R1-In and R2-In in Figure 11), and Figures 12b and 12d give the mean I/F only outside (R1-N and R2-N).

hand, the increase in I/F at small phase angles is clearly presented (Figure 12d), which is expected from the lunar surface scattering behavior. It is consistent with clear backscattering dominances of Mars with thin atmosphere in the Hubble Space Telescope data [*Soderblom et al.*, 2006]. I/F from the bottom of the canyon detected during orbit 471 also shows a backscattering component, while the reflectance of the haze displays no clear dependence on phase angle (Figure 12c). The effect of the thick dust haze on the angular dependence of its reflectance surpasses those of the surface.

4.4. Height of the Haze

[33] The height of the haze is derived using a high-resolution digital terrain model (DTM) produced from the HRSC stereo data of orbit 438. We found that the edge of the haze where it contacts the north wall can be identified as pixels of $0.0445 < I/F < 0.0460$ in the blue image (Figure 13). The surface is usually dark and little contrast in the blue images, therefore it is easier to distinguish haze using I/F in this channel than with the other color images. The edge of the haze against the southern wall is difficult to define due to direct sunlight and so only the height on the northern wall was calculated. Using this method even in the north, it is possible that some pixels representing the surface could be mistaken for haze since the topography of the canyon wall causes reflections that can fall inside of the I/F range. To obtain a conservative estimate of the haze altitude, when several "in range" pixels are at the same longitude, we measured the height of the southern most pixel (i.e., the one furthest from the wall) as the main haze edge. Figure 14 shows a cross section of the north wall of the canyon at longitude of 302°E. The arrows represent the boundary of the haze. The height along the longitude is given in Figure 15. The mean height is -4172 ± 531 m, i.e., about 1–2 km above the height of the bottom of the canyon.

4.5. Optical Depth

[34] The optical depth (τ) of the haze for both data sets (HRSC and OMEGA) was derived by using Spherical Harmonics Discrete Ordinates Model (SHDOM), a multiple scattering radiative transfer code [*Evans*, 1998]. We have considered the atmosphere as a single layer of dust particles. The code requires as input the observational geometry (provided by HRSC and OMEGA), the dust optical properties, and the contribution of the radiation reflected by the surface to the total reflectance.

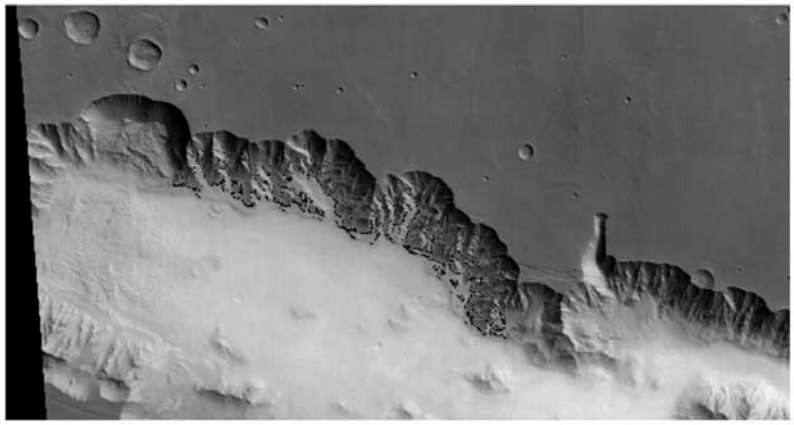

Figure 13. The HRSC blue image of orbit 437 with the haze edge against the northern wall of Valles Marineris. The edge was defined as $0.0445 < I/F < 0.0460$.

[35] We have considered three aerosol scattering models after *Markiewicz et al.* [1999] (Model M), *Tomasko et al.* [1999] (Model T) and *Ockert-Bell et al.* [1997] (Model O). The first two models were derived from observations with the Imager for Mars Pathfinder (IMP). The first used images along the great circle joining the north and south horizons to the zenith, while the second used sky surveys images at a constant elevation. The third was derived from Viking Lander, Phobos-2, and telescopic measurements. *Markiewicz et al.* [1999] obtained the dust size distribution as the effective particle radius (r_{eff}) of 1.60 μm and the effective variance (ν_{eff}) of 0.15 at $\lambda = 0.67$ μm with the modified gamma size approximation, while *Tomasko et al.* [1999] derived $r_{eff} = 1.6 \pm 0.15$ μm with a fixed ν_{eff} of 0.2 or 0.5. *Ockert-Bell et al.* [1997] employed $r_{eff} = 1.85$ μm and $\nu_{eff} = 0.51$ derived by *Pollack et al.* [1995]. All particle sizes indicated are also consistent with other results in the literature [e.g., *Chassefière et al.*, 1995] obtained $r_{eff} = 1.3-1.9$ μm from observations of Phobos-2. With Model M, we use the phase function that *Markiewicz et al.* [1999] derived directly from the IMP data, while for Models T and O, we approximate the phase functions with the one-term Henyey-Greenstein model using their asymmetry factors (Figure 16). This approximation fits the originally retrieved phase functions poorly in the forward scattering peak ($g > \sim 150°$) and not very well in the backward scattering region ($g < \sim 30°$); nevertheless this little affects the retrieval of optical depth in our case, mainly because the Henyey-Greenstein phase function is a good approximation to the true function for phase angles within the range corresponding to our observations ($38° < g < 65°$). The Henyey-Greenstein phase functions of Models T and O provide a rather similar phase function in the range of these observed phase angles, although they are larger that from Model M. The dust single scattering albedo (ϖ) and the asymmetry factor (θ) of the phase functions are shown in Figure 17. The single scattering albedo interpolated at $\lambda = 0.675$ μm after Model T ($\varpi = 0.95$) is 2% larger than the others ($\varpi = 0.93$). Considering also the difference in the single scattering albedo, the dust particles of Model M less effectively scatter than those of the other two dust models for our observational geometries. Model O provides dust optical properties in a wavelength range containing OMEGA spectral coverage completely. For applying Models M and T, we need to expand the wavelength range. On the basis of results from the analysis of observations Thermal Emission Spectrometer (TES) on board Mars Global Surveyor (MGS) [*Clancy et al.*, 2003], we have assumed that ϖ and θ remain constant for $\lambda > 0.965$ μm.

[36] We estimated the Lambertian albedo (A_L) of the surface below the haze with data taken after the haze disappeared on orbits 471 and 482 for HRSC and OMEGA, respectively. In reality the surface is not Lambertian, as it is shown in Figure 12d. Although the HRSC nadir and two stereo channel data are available, three data points are not enough to derive an accurate surface phase function. However, we focus here on the haze optical depth and, as the observational geometries for the two pairs of orbits 438–471 (HRSC) and 438–482 (OMEGA) are similar, the effect of considering a surface different from Lambertian on the derived τ is small. This is similar to considering the derived A_L as some effective albedo for the specific observation geometry. First we estimated A_L by assuming dust-free atmosphere in the data taken on orbits 471 and 482. Hereafter the models with this Lambert albedo and the three aerosol models are referred to as Models M-1, T-1 and O-1. The uncertainty from the assumption should be also considered since (1) dust particles are always suspended in this

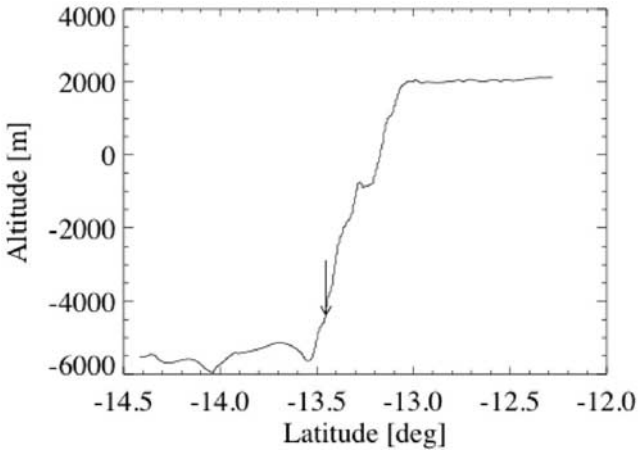

Figure 14. Cross section of the DTM along the longitude of 302°E. The arrow indicates the border of the haze.

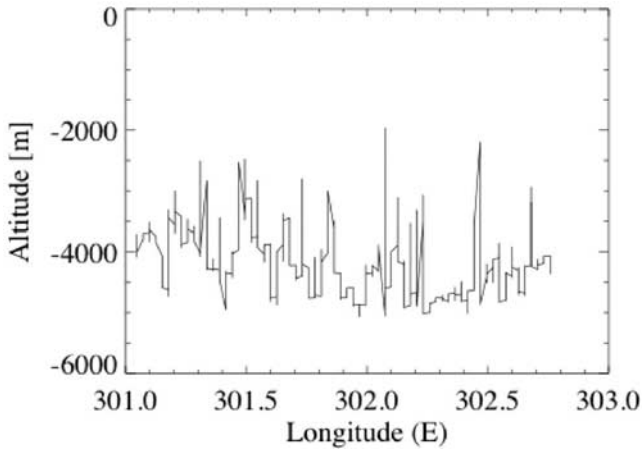

Figure 15. Altitude of the main haze edge against the northern wall detected on orbit 438. The mean height is −4172 ± 531 m.

region and (2) dust above dark surfaces such as at the bottom of Valles Marineris usually enhances the total reflectance. Therefore we adopted $\tau = 0.5$ as a reasonable optical depth and 1.0 as a dusty case at $\lambda = 0.67$ μm to estimate the range of Lambert albedo. The models with these A_L values and the three aerosols models are referred as Models M-2, T-2 and O-2 for $\tau = 0.5$ and M-3, T-3, and O-3 for $\tau = 1.0$. The applied models are summarized in Table 2.

[37] Whereas HRSC has the ability to measure at the same wavelength in the five panchromatic channels (therefore providing reflectance at different phase angles), OMEGA measures simultaneously at 352 wavelengths, providing different wavelength information. We describe below the method used for each data set and the derived optical depth.

4.5.1. Retrieval of Optical Depth With HRSC Data

[38] We analyzed the HRSC panchromatic channels to estimate the optical depth of the dust haze. The Lambert albedo of the surface below the haze is calculated from the averaged reflectance at the bottom of the canyon in region 2 obtained on orbit 471, when the atmosphere was relatively clear. The estimated A_L from the data of S1, nadir and S2 are 0.16, 0.15 and 0.17, respectively. In order to derive the optical depth for the haze, we only use A_L derived for the nadir channel.

[39] First we applied Model M-1. Figure 18a shows the results of the I/F simulations using $A_L = 0.15$ for optical depths from 0 to 5, together with the observed I/F in region 1 acquired during orbit 438. A unique optical depth does not simultaneously fit all the panchromatic data well. In this case, the nadir data suggests that the dust haze τ_m is 3.6, while the S1 data at a larger phase angle shows smaller optical depth ($\tau_m = 3.0$) and the S2 data at a smaller phase angle is better fitted with $\tau_m = 4.6$. This could be due to two effects: (1) the brightness of the surface at small (large) phase angles is actually larger (smaller) than the radiance calculated with the Lambert assumption, and/or (2) the dust particles in the canyon have a larger backscattering component than the applied phase function.

[40] Figure 18b shows the contour map of I/F calculated with the geometric angles of the nadir data in region 1 of orbit 438. The incidence angle (i) is 49.4 degrees, $e = 3.79$ degrees, and $g = 46.0$ degrees. Applying Model M-2, which assumed the optical depth is 0.5 on orbit 471, A_L is 0.14, and the observed I/F of 0.142 corresponds to $\tau_m = 3.7$. The minimum τ_m is 3.6 with $A_L = 0.15$. The maximum could be 5.0 if $A_L = 0.0$; however, even when we assume dusty atmosphere on orbit 471 (Model M-3), $A_L = 0.12$ and $\tau_m = 3.9$. Hence hereafter we consider that the maximum τ_m is derived with Model M-3.

[41] In the same manner, Models T and O are also applied. The results are shown in Figures 18c and 18d and Figures 18e and 18f, respectively. The estimated optical depths are smaller than Model M, which less effectively scatters for this wavelength and geometry than the others. The optical depth of the dust haze on orbit 438 derived with Model T is within the range from 1.7 ($A_L = 0.15$ with Model T-1) to 2.3 ($A_L = 0.08$ with Model T-3), while that with Model O is between 1.9 ($A_L = 0.15$ with Model O-1) and 2.5 ($A_L = 0.08$ with Model O-3) (Table 2). Taking into account that the main difference between three dust models comes from the different single scattering albedos, it is understandable that τ_m is larger than τ_t; however, the former should be similar to τ_o. We derive τ_m larger than τ_o because the aerosol phase function of Model M is slightly larger than Model O for the phase angles of our observations. These tests show the retrieval of the optical depth to be very sensitive to the aerosol model used, and the error in the optical depth caused by assuming Lambert albedo is smaller than the difference between the optical depths derived with each scattering model.

4.5.2. Retrieval of Optical Depth With OMEGA Data

[42] We have derived the optical depth for the haze detected on orbit 438 at wavelengths from 0.6 to 2.5 μm from OMEGA data with a similar approach. We averaged the radiance for each spectrum from measurements taken over the bottom of the canyon from 13.76°S–14.12°S and 301.7°E–302.6°E for orbit 438, and from 12.57°S–12.96°S and 296.9°E–297.8°E for orbit 482. The average reflec-

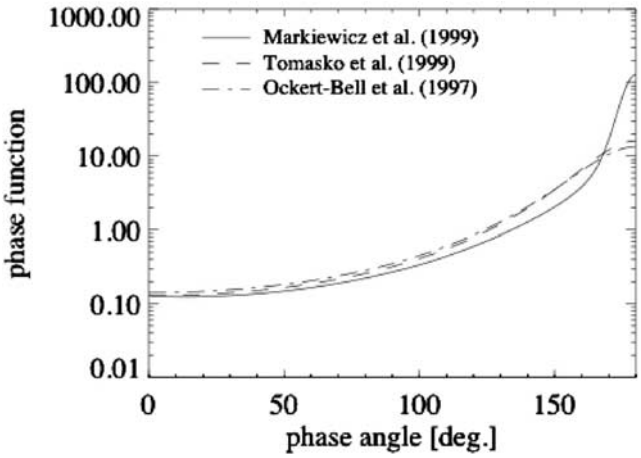

Figure 16. The solid line is for the phase function of dust particles presented by *Markiewicz et al.* [1999]. The dashed and the dot-dashed lines are the Henyey-Greenstein phase function with the asymmetry factors after *Tomasko et al.* [1999] and *Ockert-Bell et al.* [1997]. All phase functions are calculated at the wavelength of 0.675 μm.

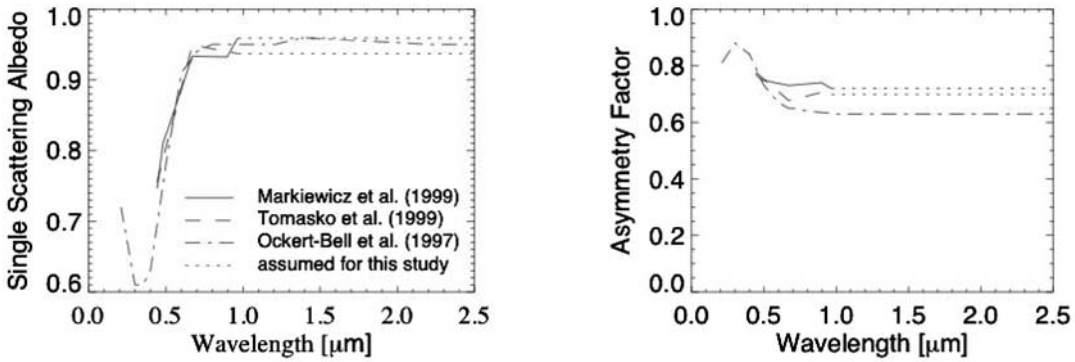

Figure 17. (left) Single scattering albedos of dust particles and (right) asymmetry factors of dust phase functions. The solid line is after *Markiewicz et al.* [1999], the dashed line is after *Tomasko et al.* [1999], and the dot-dashed line is after *Ockert-Bell et al.* [1997]. The dotted lines are assumed for this study.

tance spectra for both orbits and those corrected for the incidence angle are shown in Figure 19.

[43] The optical depths on orbit 482 (after the dust haze disappeared) are assumed to be 0.5 for Models M-2, T-2 and O-2, and 1.0 for Models M-3, T-3 and O-3 at $\lambda = 0.67$ μm, and we have estimated τ for the rest of the wavelength range scaling with the extinction efficiency factor (Q_{ext}) dependence, considered constant at $\lambda > 0.965$ μm in Models M and T. The derived albedos with the dust-free assumption, Models M-2, T-2 and O-2, and Models M-3, T-3 and O-3 are given in Figure 20. The albedos derived considering dust presence in orbit 482 are smaller than the one derived using a free atmosphere (at least at $\lambda > 0.6$ μm), given Valles Marineris low albedo (relative to Mars average albedo). That means that all three types of dust enhance the reflectance. However, the effect of the dust on the albedo wavelength dependence in the case of Models O-2, O-3 and M-3 is not as expected. For example, the relative difference between the albedo of Model O-2 and that of the dust free case is around five times larger at $\lambda = \sim 2.2$ μm than at $\lambda = 0.67$ μm, and from five to six times more in the case of Models O-3 and M-3. This is not likely correct since the contribution from Martian dust in the NIR should decrease as the wavelength increases [see, e.g., *Clancy et al.*, 2003, Figure 7a; *Drossart et al.*, 1991, Figure 4.1], and therefore the relative differences mentioned above should have a negative spectral slope. This unexpected behavior could be due to too high of an optical depth or to the use of dust that is too bright at $\lambda > 1.4$ μm relative to the shorter wavelengths. The case is similar for the surface albedo derived using Model M-2, although in this case the dust seems too bright for $\lambda > 0.896$ μm relative to the shorter wavelengths. The surface albedo behavior derived using Models T-2 or T-3 seems more reasonable than the one derived with the other two dust models, although the contribution from the aerosols is also slightly larger for larger wavelengths in the NIR, in particular when the assumed optical depth is 1.0, i.e., T-3. This is also an indication of the dust model being too bright or, more likely, to too large of an optical depth in those wavelengths. The reason for the latter could be an erroneous Q_{ext} at $\lambda > \sim 1.35$ μm, considered here constant but which is shown in the literature to slightly decrease toward longer wavelengths for the case of Martian dust [see, e.g., *Clancy et al.*, 2003].

[44] After deriving A_L, we have retrieved the haze optical depth detected on orbit 438 considering the nine models. First we applied Model O-1 because the scattering properties fully cover the OMEGA wavelength region. Figure 21a shows the retrieved dust optical depth for Model O-1 and the error in the results. We estimated this error by calculating the maximum and minimum optical depth at each wavelength that can be retrieved according to the optical property error range of *Ockert-Bell et al.* [1997], i.e., ±2%. The optical depth abruptly decreases from 2.5 at $\lambda = \sim 0.6$ μm to 1.1 at $\lambda = 1$ μm. Then, it remains almost constant up to 1.25 μm and smoothly decreases beyond to a value of 0.6 at $\lambda = 2.5$ μm. This optical depth is inconsistent with Q_{ext} provided by *Ockert-Bell et al.* [1997]. By defini-

Table 2. Applied Scattering Models and the Derived Optical Depth of the Haze With HRSC[a]

Model	τ at $\lambda = 0.67$ on Orbit 471	A_L at $\lambda = 0.67$	Haze τ at $\lambda = 0.67$ With HRSC ND Data	Reference
M-1	0.0	0.15	3.6	*Markiewicz et al.* [1999]
M-2	0.5	0.14	3.7	*Markiewicz et al.* [1999]
M-3	1.0	0.12	3.9	*Markiewicz et al.* [1999]
T-1	0.0	0.15	1.7	*Tomasko et al.* [1999]
T-2	0.5	0.13	1.9	*Tomasko et al.* [1999]
T-3	1.0	0.08	2.3	*Tomasko et al.* [1999]
O-1	0.0	0.15	1.9	*Ockert-Bell et al.* [1997]
O-2	0.5	0.13	2.1	*Ockert-Bell et al.* [1997]
O-3	1.0	0.08	2.5	*Ockert-Bell et al.* [1997]

[a]Notes: τ and λ denote the optical depth and the wavelength in units of μm.

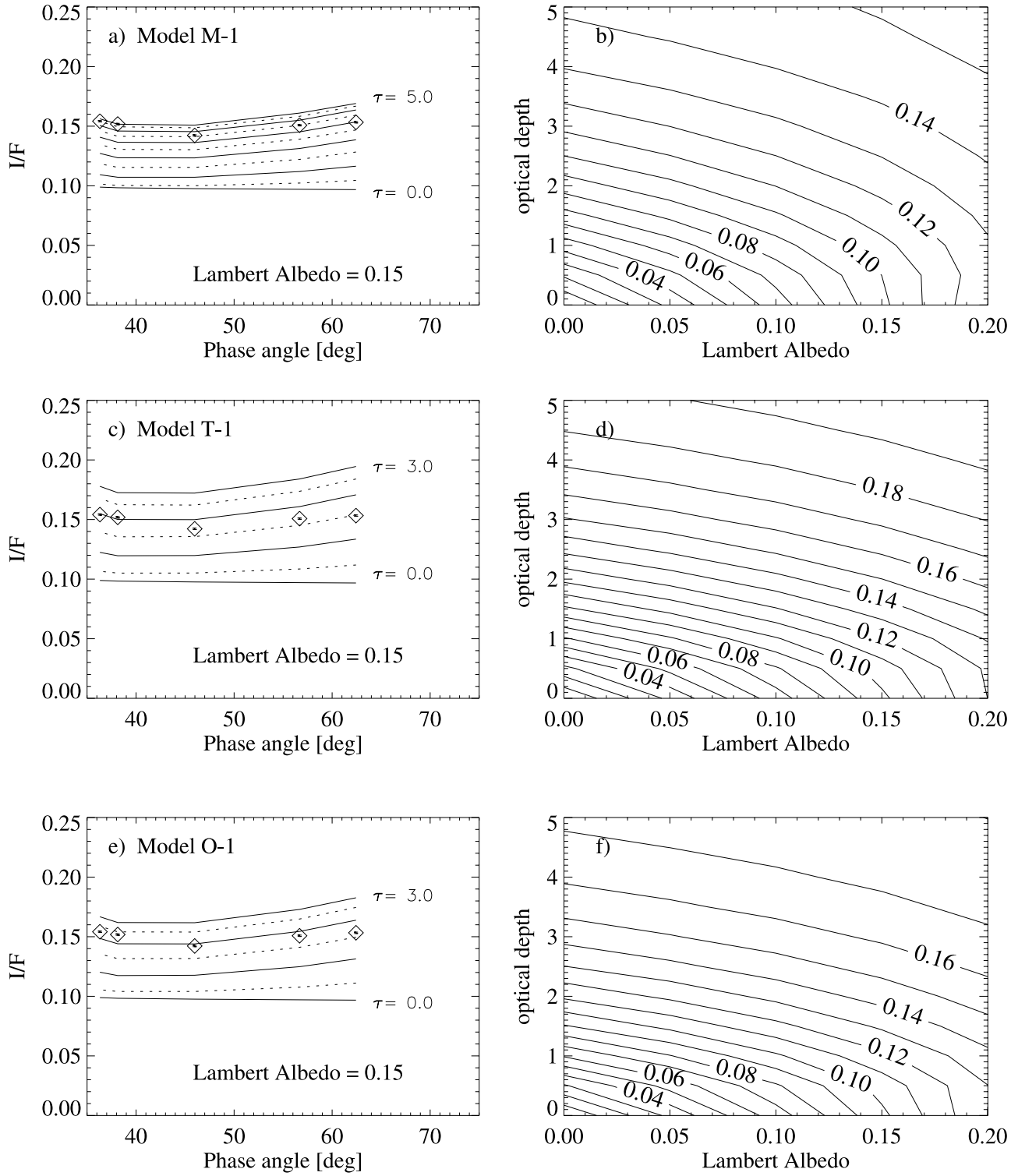

Figure 18. (a, c, and e) I/F calculated at various optical depths (τ) (lines) are compared with the observed I/F obtained by the HRSC panchromatic channels (diamonds). The interval of τ is 0.5, and the angular geometry follows that of each data point. The surface Lambert albedo (A_L) is 0.15. (b, d, and f) Contour maps of I/F with $0.0 < A_L < 0.2$ and $0.0 < \tau < 5.0$. The incidence angle of 49.4 degrees, the emission angle of 3.79 degrees, and the phase angle of 46.0 degrees corresponding to the geometry of the nadir channel are applied. The aerosol scattering models of *Markiewicz et al.* [1999] (Figures 18a and 18b), *Tomasko et al.* [1999] (Figures 18c and 18d), and *Ockert-Bell et al.* [1997] (Figures 18e and 18f) are employed.

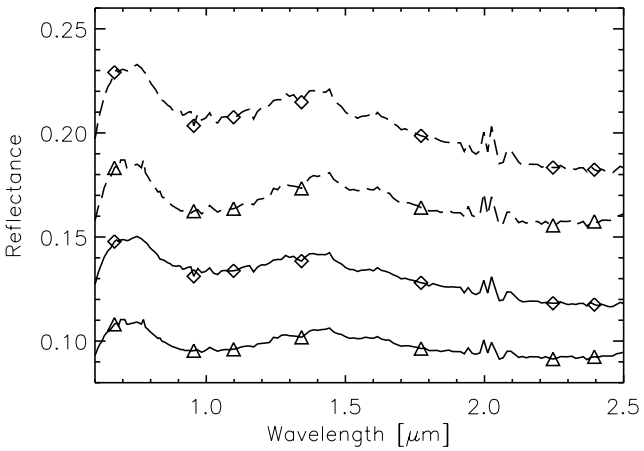

Figure 19. OMEGA average I/F (solid) and I/(F × cos(*i*)) (dashed) spectra for orbits 438 (diamonds) and 482 (triangles) inside a 0.4° × 1° box in Valles Marineris. The feature exhibited at 1.5 μm results from an instrumental effect due to the nonlinearity of the detector. The spectra are atmospherically corrected. Nevertheless, some artifacts are still present in the 2.0 μm wavelength region due to strong CO_2 absorption bands.

tion, τ must scale linearly with Q_{ext}, i.e., the ratio τ/Q_{ext} should remain constant with wavelength. However, even within the error range, the ratio slope is clearly negative, especially at visible wavelengths (see Figure 21b).

[45] The results with Models O-2 and O-3 are shown in Figure 22a. As Model O-1, the optical depth retrieved at λ = 0.6 μm is also too large with respect to the NIR. This is better illustrated in Figure 22b, where we plot the ratio τ/Q_{ext}. Although the results improve those derived using Model O-1, τ/Q_{ext} with Model O-2 still presents a very pronounced negative slope in the visible, when it should be flat. This also happens with Model O-3. The behavior beyond 1 μm in these two cases is reasonable, since the ratio remains almost constant. Therefore the kind of dust which is present in the observed haze contributes to the total reflected radiance relatively more in the visible wavelength than the dust of Model O, i.e., its single scattering albedo/asymmetry parameter is larger/smaller in the visible wavelength (relative to those in the NIR) than Model O. In other words, the set of optical properties (single scattering albedo, phase function asymmetry parameter, and extinction efficiency factor) provided by *Ockert-Bell et al.* [1997] is not suitable for this haze in Valles Marineris for the whole wavelength range from 0.6 to 2.5 μm.

[46] Next, we applied Model M-1 in the same way. Figures 22a and 22b show the retrieved optical depth and the ratio of τ/Q_{ext}, respectively. At 0.675 μm, the optical depth equals 4.1 and doubles that derived with Model O-1, and, at 0.965 μm, it is 1.5, i.e., about 30% larger than with Model O-1. In the NIR, it remains almost constant, with a local maximum at 1.35 μm and slightly decreasing beyond. However, the derived value beyond 0.896 μm is at least 2.7 times smaller than at 0.675 μm. This behavior, as it can be seen when looking at the τ to Q_{ext} ratio, is not consistent with the extinction efficiency factor provided by *Markiewicz et al.* [1999]. This could be due to dust in the canyon with an optical parameter wavelength dependence different from that of Model M, in particular, a dust darker (brighter) than Model M at wavelengths larger (smaller) than 0.896 μm. The haze optical depth derived by applying Models M-2 and M-3, although larger in the NIR (10 to 25%) for M-2 and in the whole wavelength range for M-3 (7% in the visible and up to 70% in the NIR), present a similar wavelength dependence to that with Model M-1.

[47] We finally derived the optical depth of the haze inside Valles Marineris with Models T-1, T-2 and T-3. The results are shown in Figures 22a and 22b. The optical depth of the haze when using Model T-1 is slightly smaller at $\lambda \sim$ 0.6 μm, similar at 0.7 μm and almost a factor of 2 larger in the NIR than that derived with model O-1. Besides, the maximum found in the optical depth, located at λ = $\sim$1.35 μm, is more typical for the aerosol size distributions usually measured in Mars [e.g., *Clancy et al.*, 1995; *Drossart et al.*, 1991]. Therefore Model T-1 provides a more reasonable optical depth wavelength dependence. This better behavior of Tomasko-like-dust is also illustrated in Figure 22b, which shows that the ratio between τ and Q_{ext} remains constant with wavelength within a 20% range (whereas that range was 50% with Model O-1). It is important to point out that the ratio decreases monotonically toward longer wavelengths in the NIR, which could be an indication of an incorrect assumption of constant optical properties in the whole NIR. This could be balanced with a decrease (or increase) in the single scattering albedo (or of the asymmetry parameter) in the NIR. It should also be noted that we have also considered an extinction efficiency factor that is constant with wavelength, which is very likely not to be a good assumption (but it should decrease with wavelength in the NIR). Those two factors could decrease the slope of the ratio at λ > 1.35 μm.

[48] The results with Model T-2 and T-3 are also shown in Figure 22a. The results for the optical depth in these cases are within 10% and 35%, respectively, of the ones derived with Model T-1. The ratios of optical depth to extinction

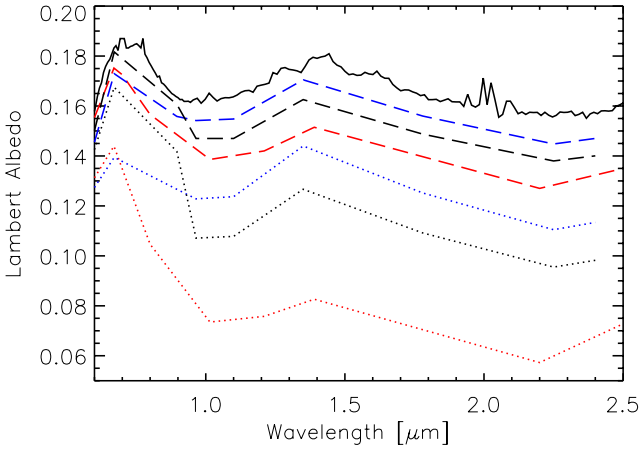

Figure 20. Lambert albedo derived from OMEGA data for orbit 482 (solid, considering an aerosol-free scenario; dashed, considering an optical depth of 0.5; dotted, considering an optical depth of 1.0 and assuming dust properties after *Ockert-Bell et al.* [1997] (red), *Markiewicz et al.* [1999] (black), and *Tomasko et al.* [1999] (blue)).

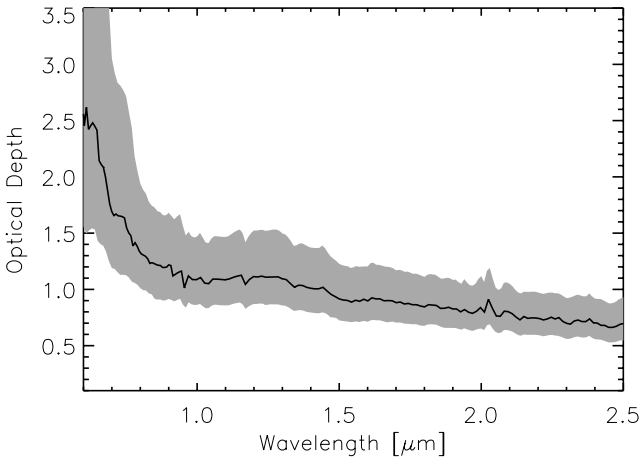

Figure 21a. Dust optical depth (solid line) for orbit 438 using *Ockert-Bell et al.* [1997] optical properties and an albedo derived from orbit 482 assuming a Lambertian-surface and aerosol-free scenario. The shadowed region shows the error in the optical depth calculated with the error range in the dust single scattering albedo and phase function asymmetry parameter provided by Ockert-Bell.

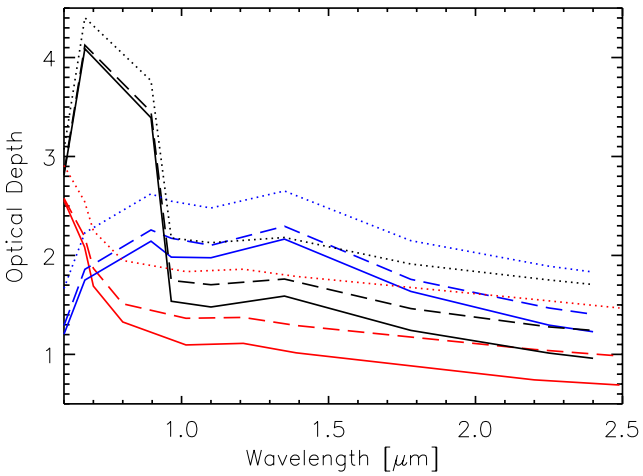

Figure 22a. Optical depth retrieved from OMEGA data for orbit 438 inside Valles Marineris. The symbols (grouped in pairs) correspond to the three different dust models used: *Ockert-Bell et al.* [1997] (red), *Markiewicz et al.* [1999] (black), and *Tomasko et al.* [1999] (blue). For each of three aerosol models assumed, the optical depths were obtained using an input Lambert albedo derived from orbit 482 under three different cases: assuming an aerosol-free scenario (solid), and assuming optical depths of 0.5 (dashed) and 1.0 (dotted) at 0.675 μm (see text).

efficiency (shown in Figure 22b), however, show a worse behavior than with Model T-1.

5. Conclusions

[49] A haze was observed in Valles Marineris at $L_s \sim 40°$ with HRSC and OMEGA on Mars Express. The existence of multiangle and multispectral imaging for this haze allows haze thickness, composition, and altitude to be determined, and models of aerosol optical properties to be tested. The haze was observed to be brighter than the bottom of the canyon in visible wavelengths. The brightness decreased within three days and the haze disappeared after nine days. The spectrometer detected no H_2O ice or CO_2 ice in absorption bands. The spectral slope in NIR, however, indicates dust loading in the valley. The brightness temperature of the feature is 223.77 ± 0.53 K. Therefore the composition of the haze was dust.

[50] Comparisons of reflectance detected with both instruments are useful for their cross calibrations. OMEGA observes nadir in the nominal mode, while HRSC nine channels point forward and backward along the orbit track. Also the panchromatic channels have wide filters at a center wavelength of 0.675 μm, where the reflectance of the Martian surface increases with wavelength steeply. Therefore direct comparison requires careful consideration of the scattering behavior of the surface and the atmosphere. The

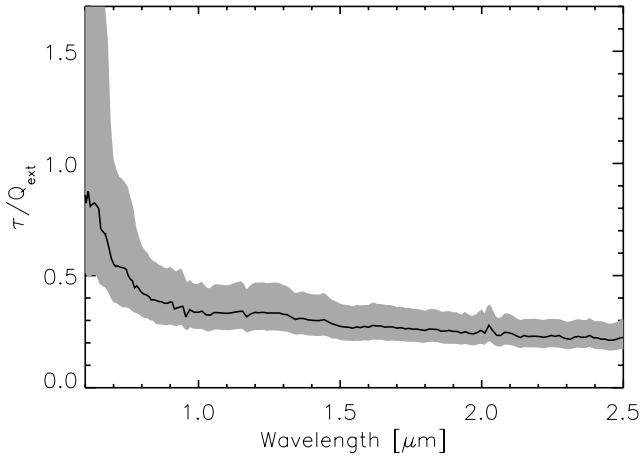

Figure 21b. Ratio between Ockert-Bell-like dust optical depth (shown in Figure 21a) and Ockert-Bell's extinction coefficient for orbit 438. The shadowed area shows the estimated error in the ratio assuming Ockert-Bell's optical parameter errors.

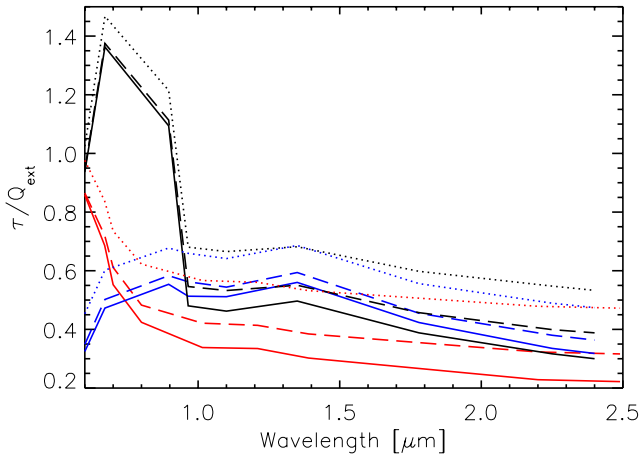

Figure 22b. Ratio between the retrieved optical depth for orbit 438 shown in Figure 22a and the extinction coefficient. The color and the style of lines denote the same in Figure 22a.

HRSC Red I/F is larger than the OMEGA I/F, which is consistent with the results of *McCord et al.* [2007]. The ratio of HRSC I/F to OMEGA I/F is 1.23, while the previously reported value is 1.10. We attribute the difference to the scattering behavior with the different geometric angles. Although there are slight shifts between the HRSC Green and Red from the OMEGA spectra, we conclude that the measurements of the two instruments are in agreement.

[51] The characteristics of the dust layer are as follows:

[52] 1. It is redder in the visible rage than the surface below. The ratio of the reflectance at $\lambda = 0.75$ μm to that at $\lambda = 0.44$ μm in the haze is 18% larger than that of the surface.

[53] 2. It reflects diffusively relative to the surface that more effectively back scatters. Hence the reflectance of the dust haze has a clear emission angle dependence, while that of the surface depends more on the phase angles.

[54] 3. The haze appeared below the altitude of -4200 ± 500 m. The haze seems to be concentrated within lowest two km of the atmosphere within the canyon.

[55] 4. It presents a negative spectral slope in the NIR (1.26 relative to 2.5 μm) with10–20% larger than that of the surface.

[56] We estimated the optical depth of the haze from the both the HRSC and OMEGA images using SHDOM. Although the surface does not scatter diffusively, the limited number of angular data points from the stereo channels are not enough to derive a surface phase function. Hence we considered the surface to be Lambertian. Three separate estimates of the Lambert albedo (A_L) were derived assuming that after the haze disappeared (1) the atmosphere was dust-free, (2) the optical depth of the atmosphere was 0.5 at $\lambda = 0.67$ μm, and (3) that was 1.0 at $\lambda = 0.67$ μm. The retrieval of optical depth is sensitive to aerosol scattering model used. The phase function of *Markiewicz et al.* [1999] represents a measured angular dependence of reflectance that differs from the one-term Henyey-Greenstein models using asymmetry factors taken from *Tomasko et al.* [1999] and *Ockert-Bell et al.* [1997] especially in the forward ($g > \sim 150°$) and backward ($g < \sim 30°$) scattering ranges. None of them, however, were able to fit all the HRSC stereo data simultaneously with the Lambertian approximation, which indicates that (1) the surface below the haze is non-Lambertian and/or (2) the dust particles in Valles Marineris have larger backscattering components than the phase functions we used. The dust scattering properties after *Ockert-Bell et al.* [1997] and *Markiewicz et al.* [1999] provided unexpected inconsistencies between τ and Q_{ext} in the near infrared and visible region, respectively. It is more suitable to apply the single scattering albedo and the phase function of dust particles derived by *Tomasko et al.* [1999] from IMP on the Mars Pathfinder to the observed dust haze, although the wavelength coverage is limited. From the HRSC nadir data, $\tau = 1.7–2.3$ at $\lambda = 0.67$ assuming the $A_L = 0.08–0.15$. From the OMEGA spectral data, by fixing a constant single scattering albedo and an asymmetry factor in the NIR, we found that the optical depth increases with increasing wavelength, with a maximum value of 2.2–2.6 at $\lambda = 1.35$ μm, then decreases to 1.2–1.8 at $\lambda = 2.4$ μm.

[57] **Acknowledgments.** We thank the HRSC Experiment Teams at DLR Berlin and Freie Universität Berlin as well as the Mars Express Project Teams at ESTEC and ESOC for their successful planning and acquisition of data as well as for making the processed data available to the HRSC Team. We acknowledge the effort of the HRSC Co-Investigator Team members and their associates who have contributed to this investigation in the preparatory phase and in scientific discussions within the team. We thank the OMEGA team at Institut d'Astrophysique Spatiale (University Paris Sud). We would like to thank Francois Forget and Stéphane Erard for reviews that greatly improved this paper. This work was partially supported by JSPS Postdoctoral Fellowships for Research Abroad (A.I.), by a NASA Mars Data Analysis Program grant to Caltech (A.I.), and by the German Aerospace Center (DLR) under contract RD-RX/50QM0011/7A (M.G.C.).

References

Bell, J. F., W. M. Calvin, M. E. Ockert-Bell, D. Crisp, J. B. Pollack, and J. Spencer (1996), Detection and monitoring of H_2O and CO_2 ice clouds on Mars, *J. Geophys. Res.*, *101*(E4), 9227–9237.

Bibring, J.-P. (2004), OMEGA: Observatoire pour la Minéralogie, l'Eau, les Glaces et l'Activité, *Eur. Space Agency Spec. Publ.*, *ESA-SP 1240*, 37–49.

Bibring, J. P., et al. (2004), Perennial water ice identified in the south polar cap of Mars, *Nature*, *428*(6983), 627–630.

Bibring, J. P., et al. (2006), Global mineralogical and aqueous Mars history derived from OMEGA/Mars express data, *Science*, *312*(5772), 400–404.

Bonello, G., J. P. Bibring, A. Soufflot, Y. Langevin, B. Gondet, M. Berthe, and C. Carabetian (2005), The ground calibration setup of OMEGA and VIRTIS experiments: Description and performances, *Planet Space Sci*, *53*(7), 711–728.

Chassefière, E., P. Drossart, and O. Korablev (1995), Post-Phobos model for the altitude and size distribution of dust in the low Martian atmosphere, *J. Geophys. Res.*, *100*(E3), 5525–5540.

Clancy, R. T., S. W. Lee, G. R. Gladstone, W. W. McMillan, and T. Rousch (1995), A new model for Mars atmospheric dust based upon analysis of ultraviolet through infrared observations from Mariner 9, Viking, and Phobos, *J. Geophys. Res.*, *100*(E3), 5251–5263.

Clancy, R. T., M. J. Wolff, and P. R. Christensen (2003), Mars aerosol studies with the MGS TES emission phase function observations: Optical depths, particle sizes, and ice cloud types versus latitude and solar longitude, *J. Geophys. Res.*, *108*(E9), 5098, doi:10.1029/2003JE002058.

Clark, R. N. (1981), Water frost and ice: The near-infrared spectral reflectance 0.65–2.5 μM, *J. Geophys. Res.*, *86*(4), 3087–3096.

Combes, M., et al. (1991), Martian atmosphere studies from the ISM experiment, *Planet. Space Sci.*, *39*(1–2), 189–197.

Drossart, P., J. Rosenqvist, S. Erard, Y. Langevin, J. P. Bibring, and M. Combes (1991), Martian aerosol properties from the Phobos ISM experiment, *Ann. Geophys.*, *9*(11), 754–760.

Erard, S., J. Mustard, S. Murchie, J. P. Bibring, P. Cerroni, and A. Coradini (1994), Martian aerosols: Near-infrared spectral properties and effects on the observation of the surface, *Icarus*, *111*(2), 317–337.

Evans, K. F. (1998), The spherical harmonics discrete ordinate method for three-dimensional atmospheric radiative transfer, *J. Atmos. Sci.*, *55*(3), 429–446.

Forget, F., A. Spiga, B. Dolla, S. Vinatier, R. Melchiorri, P. Drossart, A. Gendrin, J.-P. Bibring, Y. Langevin, and B. Gondet (2007), Remote sensing of surface pressure on Mars with the Mars Express/OMEGA spectrometer: 1. Retrieval method, *J. Geophys. Res.*, *112*, E08S15, doi:10.1029/2006JE002871.

Gerakines, P. A., J. J. Bray, A. Davis, and C. R. Richey (2005), The strengths of near-infrared absorption features relevant to interstellar and planetary ices, *Astrophys. J.*, *620*(2), 1140–1150.

Gwinner, K., F. Scholten, M. Spiegel, R. Schmidt, B. Giese, J. Oberst, R. Jaumann, G. Neukum, and HRSC Co-Investigator Team (2005), Hochauflösende Digitale Geländemodelle auf der Grundlage von Mars Express HRSC Daten, *Photogramm. Fernerkundung Geoinf.*, *5*, 387–394.

Hillier, J. K., B. J. Buratti, and K. Hill (1999), Multispectral photometry of the Moon and absolute calibration of the Clementine UV/VIS camera, *Icarus*, *141*(2), 205–225.

Jaumann, R., et al. (2007), The High Resolution Stereo Camera (HRSC) experiment on Mars Express: Instrument aspects and experiment conduct from interplanetary cruise through the nominal mission, *Planet. Space Sci.*, *55*, 928–952.

Jouglet, D., F. Poulet, R. E. Milliken, J. F. Mustard, J.-P. Bibring, Y. Langevin, B. Gondet, and C. Gomez (2007), Hydration state of the Martian surface as seen by Mars Express OMEGA: 1. Analysis of the 3 μm hydration feature, *J. Geophys. Res.*, *112*, E08S06, doi:10.1029/2006JE002846.

Langevin, Y., F. Poulet, J. P. Bibring, and B. Gondet (2005), Sulfates in the north polar region of Mars detected by OMEGA/Mars Express, *Science*, *307*(5715), 1584–1586.

Markiewicz, W. J., R. M. Sablotny, H. U. Keller, N. Thomas, D. Titov, and P. H. Smith (1999), Optical properties of the Martian aerosols as derived from Imager for Mars Pathfinder midday sky brightness data, *J. Geophys. Res.*, *104*(E4), 9009–9017.

McCord, T. B., et al. (2007), Mars Express High Resolution Stereo Camera spectrophotometric data: Characteristics and science analysis, *J. Geophys. Res.*, *112*, E06004, doi:10.1029/2006JE002769.

Melchiorri, R., et al. (2006), A simulation of the OMEGA/Mars Express observations: Analysis of the atmospheric contribution, *Planet. Space Sci.*, *54*(8), 774–783.

Neukum, G., and R. Jaumann (2004), The HRSC Co-Investigator and Experiment Team, HRSC: The High Resolution Stereo Camera of Mars Express, *Eur. Space Agency Spec. Publ.*, *ESA-1240*, 17–35.

Ockert-Bell, M. E., J. F. Bell, J. B. Pollack, C. P. McKay, and F. Forget (1997), Absorption and scattering properties of the Martian dust in the solar wavelengths, *J. Geophys. Res.*, *102*(E4), 9039–9050.

Pimentel, G. C., P. B. Forney, and K. C. Herr (1974), Evidence about hydrate and solid water in Martian surface from 1969 Mariner Infrared Spectrometer, *J. Geophys. Res.*, *79*(11), 1623–1634.

Pollack, J. B., M. E. Ockert-Bell, and M. K. Shepard (1995), Viking Lander image analysis of Martian atmospheric dust, *J. Geophys. Res.*, *100*(E3), 5235–5250.

Scholten, F., et al. (2005), Mars Express HRSC data processing: Methods and operational aspects, *Photogramm. Eng. Remote Sens.*, *71*(10), 1143–1152.

Smith, M. D. (2004), Interannual variability in TES atmospheric observations of Mars during 1999–2003, *Icarus*, *167*(1), 148–165.

Smith, M. D., J. C. Pearl, B. J. Conrath, and P. R. Christensen (2001), One Martian year of atmospheric observations by the Thermal Emission Spectrometer, *Geophys. Res. Lett.*, *28*(22), 4263–4266.

Soderblom, J. M., J. F. Bell, M. Y. H. Hubbard, and M. J. Wolff (2006), Martian phase function: Modeling the visible to near-infrared surface photometric function using HST WFPC2 data, *Icarus*, *184*(2), 401–423.

Tomasko, M. G., L. R. Doose, M. Lemmon, P. H. Smith, and E. Wegryn (1999), Properties of dust in the Martian atmosphere from the Imager on Mars Pathfinder, *J. Geophys. Res.*, *104*(E4), 8987–9007.

Wang, H., and A. P. Ingersoll (2002), Martian clouds observed by Mars Global Surveyor Mars Orbiter Camera, *J. Geophys. Res.*, *107*(E10), 5078, doi:10.1029/2001JE001815.

Warren, S. G. (1984), Optical constants of ice from the ultraviolet to the microwave, *Appl. Opt.*, *23*(8), 1206–1225.

Yen, A. S., B. C. Murray, and G. R. Rossman (1998), Water content of the Martian soil: Laboratory simulations of reflectance spectra, *J. Geophys. Res.*, *103*(E5), 11,125–11,133.

F. Altieri and G. Bellucci, Istituto di Fisica dello Spazio Interplanetario, INAF, I-00133, Rome, Italy.

J.-P. Bibring and F. Poulet, Institut d'Astrophysique Spatiale, CNRS/Université Paris-Sud, F-91405 Orsay Cedex, France.

M. Garcia-Comas, N. Hoekzema, H. U. Keller, and W. J. Markiewicz, Max-Plank-Institute of Solar System Research, Lindau, Germany.

K. Gwinner, Institute of Planetary Research, German Aerospace Center (DLR), Rutherfordstrasse 2, D-12489 Berlin, Germany.

A. Inada and M. I. Richardson, Geological and Planetary Sciences, California Institute of Technology, 1200 East Colorado Boulevard, M/C 150-21, Pasadena, CA 91125, USA. (inada@gps.caltech.edu)

G. Neukum, Institute of Geosciences, Freie Universität Berlin, Malteser Strasse 74-100, D-12249 Berlin, Germany.